Ferromagnetic and antiferromagnetic order in bacterial vortex lattices
Supplementary information

Hugo Wioland[1,2†], Francis G. Woodhouse[1†,3], Jörn Dunkel[4], and Raymond E. Goldstein[1]

[1]Department of Applied Mathematics and Theoretical Physics, University of Cambridge, Wilberforce Road, Cambridge CB3 0WB, U.K.

[2]Institut Jacques Monod, Centre Nationale pour la Recherche Scientifique (CNRS), UMR 7592, Université Paris Diderot, Sorbonne Paris Cité, F-75205 Paris, France

[3]Faculty of Engineering, Computing and Mathematics, The University of Western Australia, 35 Stirling Highway, Crawley, Perth WA 6009, Australia

[4]Department of Mathematics, Massachusetts Institute of Technology, 77 Massachusetts Avenue, Cambridge MA 02139-4307, U.S.A.

[†]*Present address.*

1   Experimental consistency with theoretical model

In populating our chosen theoretical models, we make important assumptions of the experimental data concerning spin bias, statistical steadiness, and phase-space exploration. In the following, we discuss these assumptions and provide evidence for their validity.

### 1.1   Absence of spin handedness bias

In the Hamiltonian (1), we assume a symmetric local quartic potential. For this to be valid, the vortices must be free of any handedness bias that might be induced by interactions between the chiral bacteria and the upper and lower surfaces of the chamber. Plotting a histogram of the time-averaged spins across all experiments shows no discernible bias towards either vorticity handedness (Supplementary Fig. 1a), so this assumption is justified.

1.2   Statistical steady state

When estimating parameters using movies taken after 4 and 8 minutes with equal weight, we are assuming that the suspension has reached a sufficiently statistically-steady state no later than 4 minutes after injection. We checked this assumption by comparing the spin–spin correlation in movies taken at 4 and 8 minutes with identically acquired movies taken 1 minute after injection. We found that the mean correlation changed much less between 4 and 8 minutes than between 1 and 4 minutes for experiments both below and above the critical transition gap size (Supplementary Fig. 1b), indicating sufficient equilibration to perform parameter estimation at both 4 and 8 minutes independently.

1.3   Phase-space exploration

A system following an equilibrium-like description such as the model in Eq. (2) will not be frozen into one configuration for all time. Rather, given sufficient time, it should explore all states of its configuration space according to a steady-state probability distribution. Our experiments show this exploration behaviour, with spins fluctuating and changing sign over time (Supplementary Fig. 1e,f). This is particularly noticeable when comparing between the same experiment at the two observation times of 4 and 8 minutes, during which time some (Supplementary Fig. 1c) or most (Supplementary Fig. 1d) spins may have changed orientation. However, the system is always exploring a distribution consistent with a particular preferred antiferromagnetic or ferromagnetic correlation, dependent on the gap size.
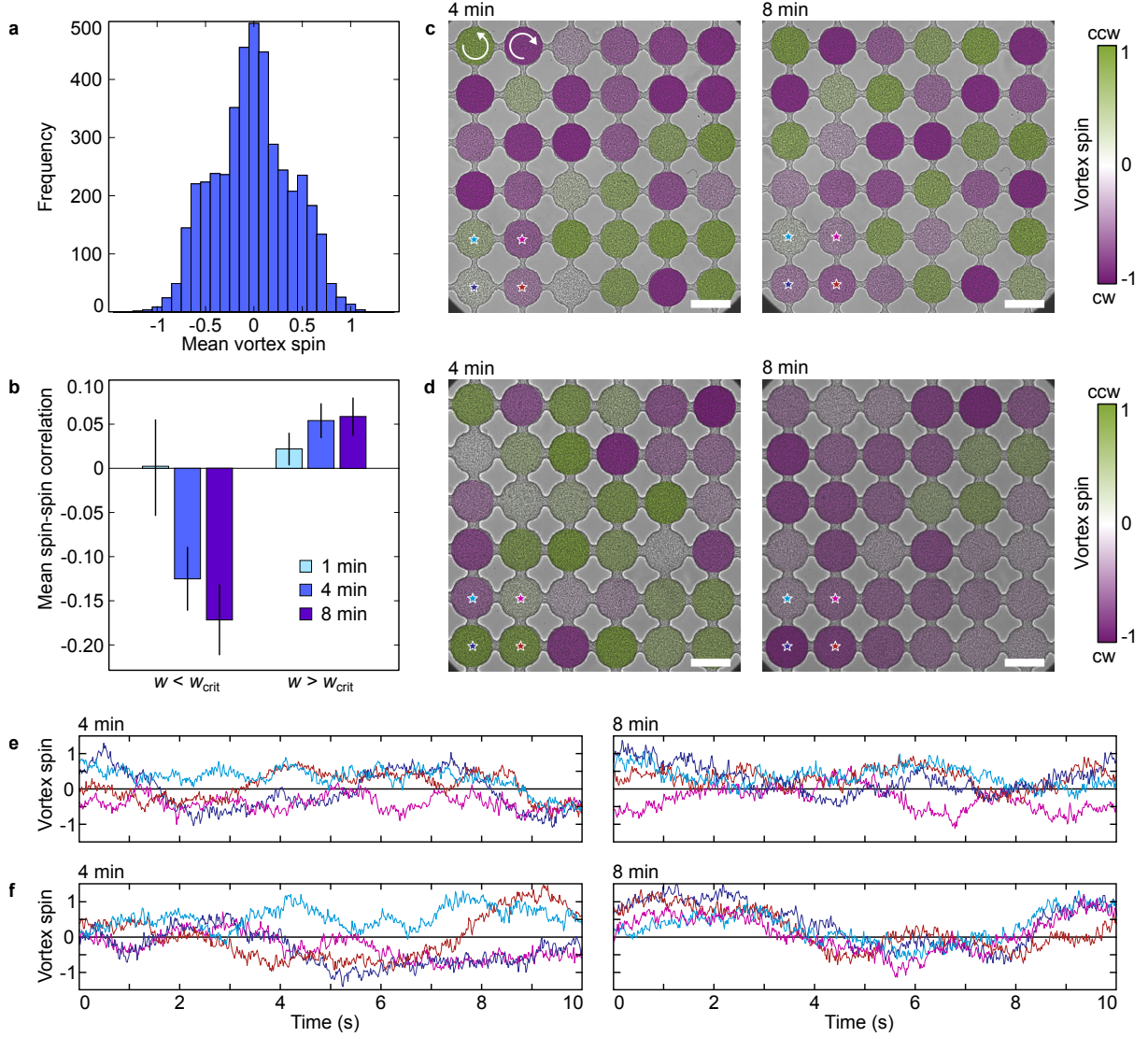
Supplementary Figure 1 – Experiments are unbiased and explore a statistical steady state. a, Histogram of time-averaged vortex spin of each cavity $\langle V_i(t) \rangle$ across all square lattice experiments, exhibiting symmetry about zero spin. **b**, Spin–spin correlation χ averaged over all movies taken 1, 4 or 8 min after injection, categorised by gap size $w < w_{\mathrm{crit}}$ or $w > w_{\mathrm{crit}}$. The suspension is not equilibrated 1 min after injection, but results are similar between 4 and 8 min indicating equilibration. **c,d**, Frames from movies taken from two experiments at 4 and 8 min, with $w = 7\,\mu\mathrm{m}$ (**c**) and $w = 11\,\mu\mathrm{m}$ (**d**), showing phase-space exploration between the observation times. **e,f**, Spin–time traces of four adjacent vortices from the experiments shown in **c,d** (line colours correspond to star colours in **c,d**).

2 Parameter inference under the full model

For a given sequence of discrete experimental observations $\{\mathbf{V}(t), \mathbf{P}(t)\}_{t=n\Delta t}$ derived from one movie with constant time step $\Delta t = 1/60$ s and rescaled by $\overline{U}$ (Methods), we wish to estimate the most likely parameter values assuming the SDE model (2) holds. We do this by first discretizing Eq. (2) and then applying linear regression. First, the rescaling by $\overline{U}$ used to eliminate variable oxygenation effects (Methods) implies that we must also rescale the time step to $\delta t = \Delta t/\tau$, where $\tau = \ell/\overline{U}$ is a time scaling with length scale $\ell = 1\,\mu\mathrm{m}$ selected as the characteristic width of a bacterium. All parameters are subsequently dimensionless under these scalings; those for an *unscaled* experiment (denoted by tildes) with desired or observed RMS velocity $\overline{U}$ can then be recovered as $\tilde{J}_v = J_v/\tau$, $\tilde{J}_p = J_p/\tau$, $\tilde{a}_v = a_v/\tau$, $\tilde{b}_v = b_v/(\overline{U}^2\tau)$, $\tilde{a}_p = a_p/\tau$, $\tilde{T}_v = \overline{U}^2 T_v/\tau$ and $\tilde{T}_p = \overline{U}^2 T_p/\tau$. Now, using this time step,

Eq. (2) discretizes in the Euler–Maruyama scheme[1] as

$$\mathbf{V}(t + \delta t) = \mathbf{V}(t) - (\partial H/\partial \mathbf{V})_t \delta t + \sqrt{2T_v \delta t} \mathbf{N}_v, \tag{S1}$$

$$\mathbf{P}(t + \delta t) = \mathbf{P}(t) - (\partial H/\partial \mathbf{P})_t \delta t + \sqrt{2T_p \delta t} \mathbf{N}_p, \tag{S2}$$

where $\mathbf{N}_v$ and $\mathbf{N}_p$ are vectors of independent $\mathcal{N}(0,1)$ random variables. Component-wise, Eqs. (S1) and (S2) read

$$V_i(t + \delta t) = (1 - a_v \delta t)V_i(t) - b_v \delta t V_i(t)^3$$
$$+ J_v \delta t \sum_{j\,:\,V_j \sim V_i} V_j(t) + J_p \delta t \sum_{j\,:\,P_j \sim V_i} P_j(t) + \sqrt{2T_v \delta t} N_{v,i}, \tag{S3}$$

$$P_i(t + \delta t) = (1 - a_p \delta t)P_i(t) + J_p \delta t \sum_{j\,:\,V_j \sim P_i} V_j(t) + \sqrt{2T_p \delta t} N_{p,i}. \tag{S4}$$

By Eq. (S4), using data from all observation times and vortices to perform a linear regression of $P_i(t+\delta t)$ on the two variables

$$\left\{ P_i(t), \sum_{j\,:\,V_j \sim P_i} V_j(t) \right\}$$

yields estimates $\{1 - \hat{a}_p \delta t, \hat{J}_p \delta t\}$ of the variables' respective coefficients and thence estimates $\hat{a}_p$ and $\hat{J}_p$ of a_p and J_p. Next, after substituting the estimate $J_p = \hat{J}_p$ into Eq. (S3) to reduce the dimensionality, a linear regression of $V_i(t + \delta t) - \hat{J}_p \delta t \sum_{j\,:\,P_j \sim V_i} P_j(t)$ on the three variables

$$\left\{ V_i(t), V_i(t)^3, \sum_{j\,:\,V_j \sim V_i} V_j(t) \right\}$$

yields estimates $\{1 - \hat{a}_v \delta t, -\hat{b}_v \delta t, \hat{J}_v \delta t\}$ of their respective coefficients and thence estimates $\hat{a}_v$, $\hat{b}_v$ and $\hat{J}_v$ of a_v, b_v and J_v. Finally, the variances $2\hat{T}_v \delta t$ and $2\hat{T}_p \delta t$ of the residuals to the regressions in Eqs. (S3) and (S4) respectively yield estimates $\hat{T}_v$ and $\hat{T}_p$ of T_v and T_p.

Boundary terms are treated by assuming a truly finite system with free boundary conditions, effectively fixing all pillar and vortex spins at zero outside of the observed domain. Since we do not image a full 6×6 offset lattice of pillars, but instead the internal 5×5 lattice, periodic boundary conditions are not possible; indeed, for a small system, free boundaries are often preferable over periodic boundaries in general.

3 Simulations

To reconstruct the vortex–vortex correlation function $\chi(w)$ as a continuous function of gap width w, we reconstructed the parameters as functions of w from the experimental data and numerically integrated the model (2) over a range of w. The simulations can then be used to explore the system on longer time scales than possible experimentally. We discuss this process further in the following section.

3.1 Parameter reconstruction

Running the parameter estimation procedure for every suitable experimental movie (those not containing any 'locked' immobile cavities, occasionally seen at small w) results in a set of parameter estimates $\mathcal{E}_i$ at gaps w_i. Estimates for movies from the same experiment were averaged, and then placed into non-overlapping w-bins of size $2.5\,\mu$m and averaged in both w and parameter value within each bin (Supplementary Fig. 2, points). Using non-linear least-squares regression estimation, the parameters were then
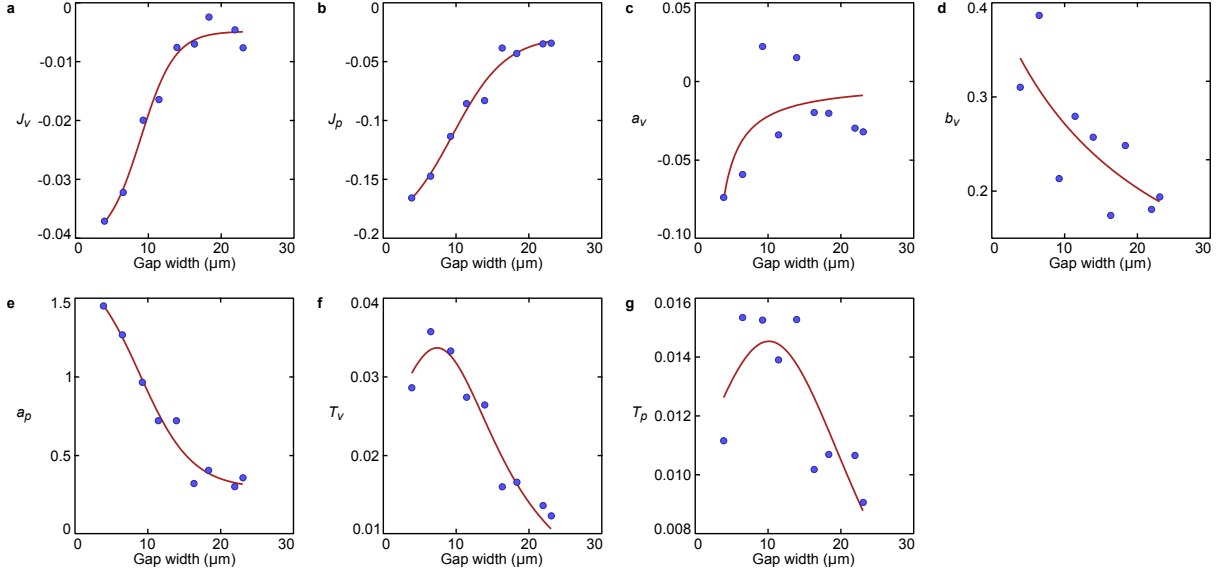
Supplementary Figure 2 – Parameters in the full model can be inferred using regression methods. Points are averages within non-overlapping $2.5\,\mu$m bins of parameters inferred for each experiment using linear regression on a discretization of Eq. (2), and lines are parametric best fits of selected functional forms to the points (Sec. 2).

fitted with chosen functional forms: J_v, J_p, a_p with a logistic function $\alpha_1 + \alpha_2/(1 + 10^{\alpha_3(\alpha_4 - w)})$; a_v, b_v with a rational function $\alpha_1/(w + \alpha_2)$; and T_v, T_p with a rational function $(\alpha_1 + \alpha_2 w)/(w^2 + \alpha_3 w + \alpha_4)$ (Supplementary Fig. 2, lines). These forms were chosen as appearing to give the best representation of the data points' behaviour (such as not introducing maxima where none are observed for J_v, J_p, a_p, and not presuming too detailed a functional form for the noisiest parameters a_v and b_v) with the fewest possible fit parameters.

3.2 Simulation method

We numerically integrated Eq. (2) using the discretization in Eqs. (S1) and (S2), wherein we set $N = 6$ and $\delta t = 1/600$ (equivalent to $1/60\,$s when $\overline{U} = 10\,\mu$m). We initialized $\mathbf{V}$ and $\mathbf{P}$ to zero, and after an equilibration period of $50/\delta t$ frames we recorded every frame. Trial and error showed an observation period of $8000/\delta t$ frames in an ensemble of 25 identical repetitions to be sufficient to obtain a stable estimate of the average vortex–vortex correlation χ. This was evaluated at each of 101 regularly-spaced values of w in the range $\min w_i \le w \le \max w_i$ (Fig. 1j).

In all simulations we use free boundary conditions (that is, setting components of $\mathbf{P}$ and $\mathbf{V}$ to zero outside of the simulation domain) consistent with the conditions used in parameter inference. Because of the small size of the system being simulated, periodic boundary conditions are inappropriate as they have too great a dynamical influence and do not reproduce the expected spin–spin correlation behaviour. Simulations on moderately larger lattices with free boundary conditions retain the same form of correlation curve as for the 6×6 grid, but as the number of grid points increases, the antiferromagnetic phase eventually disappears. This reflects the sensitivity of the system to fluctuations as vortex and pillar interactions compete near to a critical point; were experiments to be performed on larger lattices and parameters inferred from that data, this regime would reappear in simulations.

3.3 Spin fluctuations

As in the experiments, after equilibrating during the burn-in period, each simulation explores configuration space within the statistical steady state. The simulations then allow us to examine system behaviour over time scales longer than those of the experimental movies, whose durations were constrained by equipment data capacity. In particular, the simulations exhibit domain fluctuations and spin flipping
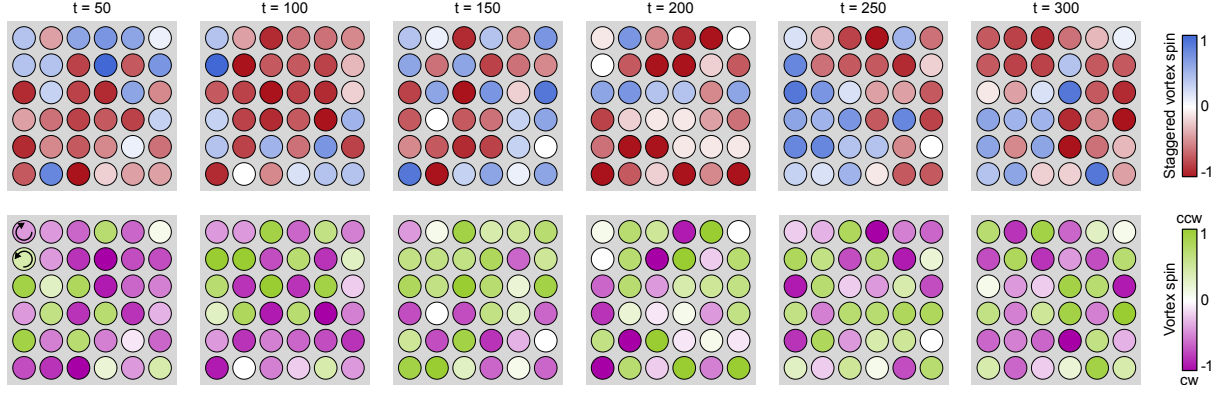
Supplementary Figure 3 – Simulations of the full model reproduce the spin-flip dynamics over long times.
Frames of a simulation using parameter values at $w = 4\,\mu\text{m}$ from the reconstructions in Supplementary Fig. 2.
Top row: staggered vortex spins, corresponding to multiplying each spin site alternately by ± 1 to show coherent antiferromagnetic domains as single colours. Bottom row: unstaggered vortex spins. Domain fluctuations and large-scale spin flips can be seen over the simulation at times extending to an equivalent of double or triple the lengths of typical observations.

as observed in the experiments (Supplementary Fig. 1c–f), while better demonstrating the system fully exploring configuration space. Supplementary Fig. 3 depicts a simulation using reconstructed parameter values at $w = 4\,\mu\text{m}$, firmly inside the antiferromagnetic regime, run for a length equivalent to approximately $25\,\text{s}$ of an experiment with RMS kinetic energy $\bar{U} = 12\,\mu\text{m}\text{s}^{-1}$ (the average seen in experiments; see Methods), exhibiting dynamic configuration exploration within an equilibrium distribution favouring antiferromagnetic correlation.

4   Reduction to vortex-only model

A true Langevin equation for $\mathbf{V}$ can be obtained by integrating Eq. (2b) for $\mathbf{P}$ as a function of $\mathbf{V}$ and back-substituting[2,3]. Since Eq. (2b) is linear in $\mathbf{P}$, we have

$$P_i(t) = P_i(0)e^{-a_p t} + J_p \sum_{j:V_j \sim P_i} \int_0^t V_j(s)e^{a_p(s-t)}\,ds + \sqrt{2T_p}\int_0^t e^{a_p(s-t)}\,dW(s),$$

where the third term is an integral with respect to the standard Brownian motion $W(t)$. When $a_p t \gg 1$, the first term decays and the second can be approximated by pulling out $V_j(s)$ at $s = t$ (provided $\mathbf{V}$ varies sufficiently slowly over short time intervals), giving

$$P_i(t) \approx \frac{J_p}{a_p} \sum_{j:V_j \sim P_i} V_j(t) + \sqrt{2T_p}\int_0^t e^{a_p(s-t)}\,dW(s). \tag{S5}$$

This is valid here since $a_p \sim 1$ (Supplementary Fig. 2) and each $10\,\text{s}$ experimental movie reaches non-dimensional times $t = (10\,\text{s})/\tau \sim 100$. Thus P_i reduces to time-autocorrelated noise $\nu(t) = \sqrt{2T_p}\int_0^t e^{a_p(s-t)}\,dW(s)$ about a mean proportional to the average spin of adjacent vortices $[P_i]_V = \frac{1}{4}\sum_{j:V_j \sim P_i} V_j$; that is, $P_i \approx (4J_p/a_p)[P_i]_V + \nu$. The noise has autocorrelation

$$C(t,t') = \mathbb{E}\left[\nu(t)\nu(t')\right] = \frac{T_p}{a_p}\left[e^{-a_p|t-t'|} - e^{-a_p(t+t')}\right] \approx \frac{T_p}{a_p}e^{-a_p|t-t'|}$$

for $a_p t, a_p t' \gg 1$. In this limit, C decays rapidly away from $t = t'$, and $\nu(t)$ is approximately normally distributed at every t with variance T_p/a_p.
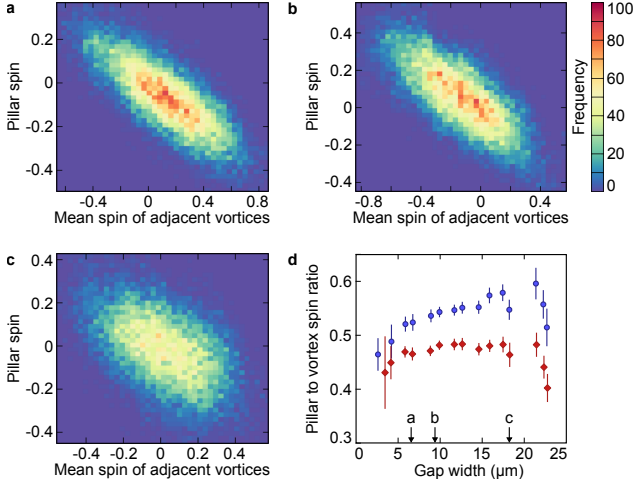
Supplementary Figure 4 – Pillar spin distributions vary linearly with the average spin of adjacent vortices. a–c, Two-dimensional histogram of $(P_i, [P_i]_V)$ from three example movies, showing uniform spread about a line $P_i \propto [P_i]_V$. Gap widths 7, 10 and 18 μm, respectively. d, The proportionality constant α, where $P_i \approx -\alpha[P_i]_V$, depends weakly on gap width. Direct correlations from data (blue circles) compare well with the theoretical result $\alpha = -4J_p/a_p$ calculated with inferred model parameters (red diamonds). Each point represents an average over ≥ 5 movies in 3μm bins at 1.5μm intervals; vertical bars indicate standard errors (Methods).

Now, in Eq. (2a), interaction with $\mathbf{P}$ arises through the term $J_p \sum_{j:P_j \sim V_i} P_j$ in $\partial H / \partial V_i$. By Eq. (S5), this approximates to

$$J_p \sum_{j:P_j \sim V_i} P_j \approx \frac{J_p^2}{a_p} \left[4V_i + 2 \sum_{j:V_j \sim V_i} V_j + \text{(n.n.n.)} \right] + J_p \sum_{j=1}^{4} \nu^{(j)}, \tag{S6}$$

where $\nu^{(j)}$ are i.i.d. noise processes as above, and 'n.n.n.' denotes next-nearest-neighbour interactions which we neglect. When substituted into Eq. (2a), each noise term contributes $J_p \nu^{(j)} dt$, which represents a contribution of the form $J_p \int_0^t \nu^{(j)}(s) \, ds$ in the formal integral representation of Eq. (2a). Inserting the definition of ν into this integral and exchanging the order of integration implies

$$J_p \int_0^t \nu^{(j)}(s) \, ds = \frac{J_p \sqrt{2T_p}}{a_p} \int_0^t [1 - e^{a_p(s-t)}] \, dW(s).$$

In our experiments, we found $|J_p/a_p| \approx 1/10$ and $T_p \lesssim T_v$ over all gap widths (Supplementary Fig. 2), so these are weak contributions to the noise in $\mathbf{V}$. Indeed, the integral has variance $t - 3/(2a_p) + O(e^{-a_p t})$ as $t \to \infty$, so for large a_p its effect can be approximated by the pure Brownian motion $\int_0^t dW(r)$ (whose variance is t). Thus the contributions $J_p \nu^{(j)} dt$ reduce to small Brownian noise terms $(J_p \sqrt{2T_p}/a_p) dW$, which combine with the existing noise into one single term $\sqrt{2T} dW$ of slightly increased temperature $T = T_v + 4T_p J_p^2/a_p^2$. Substituting Eq. (S6) into Eq. (2a) yields new approximate $\mathbf{V}$ dynamics obeying $d\mathbf{V} = -(\partial \hat{H}/\partial \mathbf{V}) dt + \sqrt{2T} d\mathbf{W}$ with effective Hamiltonian

$$\hat{H}(\mathbf{V}) = -J \sum_{V_i \sim V_j} V_i V_j + \sum_{V_i} \left(\tfrac{1}{2} a V_i^2 + \tfrac{1}{4} b V_i^4 \right),$$

where the effective coupling constants are $J = J_v + 2J_p^2/a_p$, $a = a_v - 4J_p^2/a_p$ and $b = b_v$.

Though this reduction will only be achieved exactly in the thermodynamic limit when boundary effects are eliminated, this still serves as a good approximation for a finite system. To verify this reduction with our experimental data, we compared P_i with $[P_i]_V$. Consistent with Eq. (S5), we found P_i to be linearly correlated with $[P_i]_V$ in every square-lattice experiment (Supplementary Fig. 4a–c), confirming our use of a quadratic potential for $\mathbf{P}$. Writing $-\alpha$ for the correlation coefficient, we found $\alpha \approx 0.5$ with weak dependence on the gap width; this compares well with the analytic result $\alpha = -4J_p/a_p$ from Eq. (S5) when calculated using experimentally inferred parameters (Supplementary Fig. 4d).
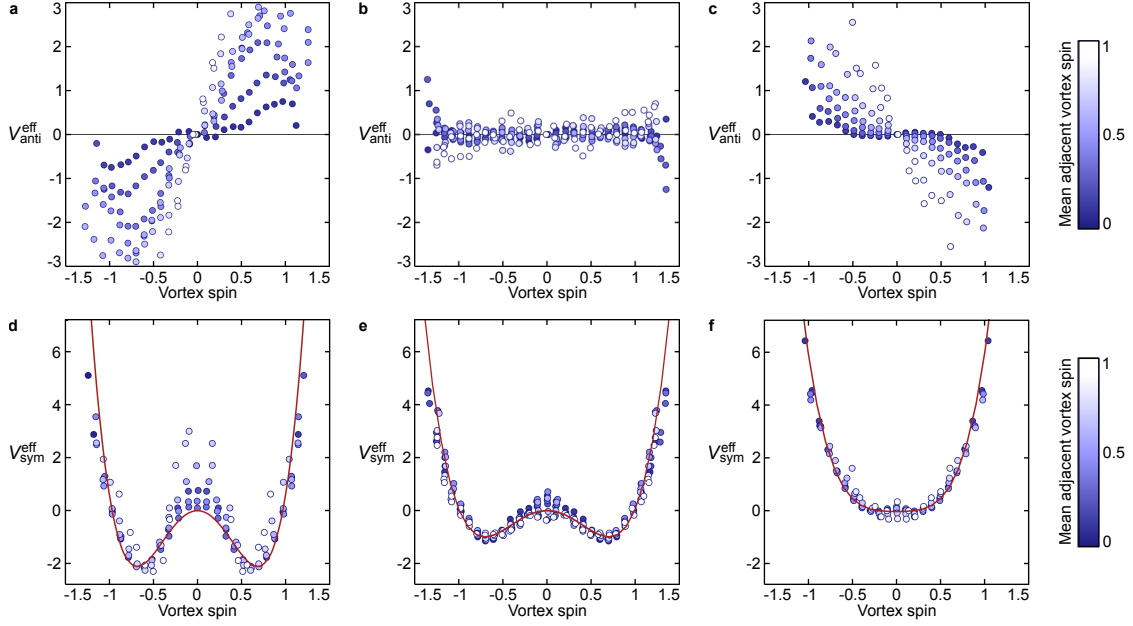
Supplementary Figure 5 – Parameters in the reduced model can be inferred by fitting effective single-spin potentials. Reduced model parameters βJ, βa and βb are estimated by fitting the antisymmetric and symmetric parts of the effective potential $\mathcal{V}^{\mathrm{eff}}(V_i \,|\, [V_i]_V)$ (Sec. 5.1). Data shown from three example movies of square lattices with gap widths $7\,\mu$m (**a,d**), $10\,\mu$m (**b,e**) and $18\,\mu$m (**c,f**). **a–c**, The antisymmetric part of the effective potential reveals the vortex–vortex coupling βJ, spanning the range $J < 0$ (**a**), $J \approx 0$ (**b**) and $J > 0$ (**c**). Estimated $\mathcal{V}^{\mathrm{eff}}_{\mathrm{anti}}$ (points), coloured by mean adjacent spin $[V_i]_V$. **d–f**, The symmetric part of the effective potential reveals the non-interacting single-spin potential, which flattens with increasing gap width. Estimated $\mathcal{V}^{\mathrm{eff}}_{\mathrm{sym}}$ (points) coloured by mean adjacent spin $[V_i]_V$, with fitted single-spin potentials (lines).

5   Parameter inference under the reduced model

5.1   Distribution fitting

We assume that $\mathbf{V}$ obeys a Boltzmann distribution $p(\mathbf{V}) \propto e^{-\beta \hat{H}(\mathbf{V})}$. The probability density $p(V_i \,|\, [V_i]_V)$ of one spin V_i conditional on the mean of its adjacent spins $[V_i]_V = \frac{1}{4} \sum_{j\,:\,V_j \sim V_i} V_j$ satisfies

$$\log p(V_i \,|\, [V_i]_V) - \log p(0 \,|\, [V_i]_V) = -\mathcal{V}^{\mathrm{eff}}(V_i \,|\, [V_i]_V), \tag{S7}$$

where we have defined the effective single-vortex potential

$$\mathcal{V}^{\mathrm{eff}}(V_i \,|\, [V_i]_V) = -4\beta J V_i [V_i]_V + \tfrac{1}{2}\beta a V_i^2 + \tfrac{1}{4}\beta b V_i^4.$$

We estimate $p(V_i \,|\, [V_i]_V)$ for each movie by forming a two-dimensional histogram in V_i and $[V_i]_V$ and then normalizing at every fixed V_i. In forming the histogram, we exploit the invariance of $\mathcal{V}^{\mathrm{eff}}$ under the transformation $V_i \to -V_i$ and $[V_i]_V \to -[V_i]_V$ to double the number of data points.

Taking the antisymmetric part $\mathcal{V}^{\mathrm{eff}}_{\mathrm{anti}} = \frac{1}{2}\left[\mathcal{V}^{\mathrm{eff}}(V_i \,|\, [V_i]_V) - \mathcal{V}^{\mathrm{eff}}(-V_i \,|\, [V_i]_V) \right]$ eliminates the non-interacting terms, so Eq. (S7) implies

$$\tfrac{1}{2}\left[-\log p(V_i \,|\, [V_i]_V) + \log p(-V_i \,|\, [V_i]_V) \right] = -4\beta J V_i [V_i]_V.$$

This allows estimation of the interaction constant βJ from the density $p(V_i|[V_i]_V)$ (Fig. 2a and Supplementary Fig. 5a–c). The symmetric part $\mathcal{V}^{\mathrm{eff}}_{\mathrm{sym}} = \frac{1}{2}\left[\mathcal{V}^{\mathrm{eff}}(V_i \,|\, [V_i]_V) + \mathcal{V}^{\mathrm{eff}}(-V_i \,|\, [V_i]_V) \right]$ eliminates the interaction term in a similar fashion, so Eq. (S7) now implies

$$\tfrac{1}{2}\left[-\log p(V_i \,|\, [V_i]_V) - \log p(-V_i \,|\, [V_i]_V) \right] + \log p(0 \,|\, [V_i]_V) = \tfrac{1}{2}\beta a V_i^2 + \tfrac{1}{4}\beta b V_i^4.$$

Typically there are fewer observations near $V_i = 0$, so $p(0 \,|\, [V_i]_V)$ can be difficult to infer directly. Instead, we adjust $\log p(0 \,|\, [V_i]_V)$ for each $[V_i]_V$ bin to minimize the difference between $\mathcal{V}_{\text{sym}}^{\text{eff}}(V \,|\, [V_i]_V)$ and $\mathcal{V}_{\text{sym}}^{\text{eff}}(V \,|\, 0)$. We then fit the remaining single vortex potential with parameters βa and βb (Supplementary Fig. 5d–f), from which we compute the spins $\pm V_{\min}$ ($V_{\min} > 0$) minimizing the local effective single-spin energy $\mathcal{V}_{\text{sym}}^{\text{eff}}$, namely

$$V_{\min} = \begin{cases} \sqrt{|a|/b} & \text{if } a < 0, \\ 0 & \text{if } a > 0, \end{cases}$$

and the effective spin-flip energy barrier

$$\mathcal{V}_{\text{sym}}^{\text{eff}}(0) - \mathcal{V}_{\text{sym}}^{\text{eff}}(\pm V_{\min}) = \begin{cases} \beta a^2/(4b) & \text{if } a < 0, \\ 0 & \text{if } a > 0, \end{cases}$$

which together characterize the single-spin symmetric quartic potential (Fig. 2b,c).

To ensure boundary conditions do not have a strong effect on the inferred parameters by comparison with those used in the SDE discretization method (see below), boundary terms are treated in this method using neighbour averaging whereby the mean adjacent spin $[V_i]_V$ is computed as an average over only two spins (in a corner) or three spins (at an edge). This corresponds to assuming that, in each computation of $[V_i]_V$, spin sites absent from the lattice are the mean of the sites present in the sum.

5.2 SDE discretization

Estimations made by the above method were verified by estimations obtained through the same SDE discretization method used in the full model. Though the absence of pillars now means periodic boundary conditions could be used, we retain the free boundary conditions to maintain consistency with the full model and for comparison with the averaging conditions used above. The components of the reduced model SDE $d\mathbf{V} = -(\partial \hat{H}/\partial \mathbf{V})dt + \sqrt{2T}\,d\mathbf{W}$ have Euler–Maruyama discretization

$$V_i(t + \delta t) = (1 - a\delta t)V_i(t) - b\delta t V_i(t)^3 + J\delta t \sum_{j \,:\, V_j \sim V_i} V_j(t) + \sqrt{2T\delta t}N_i,$$

where N_i are independent $\mathcal{N}(0, 1)$ random variables. Performing linear regression of $V_i(t + \delta t)$ on the three variables

$$\left\{ V_i(t), V_i(t)^3, \sum_{j \,:\, V_j \sim V_i} V_j(t) \right\}$$

then gives estimates $\{1 - \hat{a}\delta t, -\hat{b}\delta t, \hat{J}\delta t\}$ of the respective coefficients, from which estimates $\hat{a}$, $\hat{b}$ and $\hat{J}$ of the variables a, b and J can be deduced. The estimate $\hat{T}$ of the fluctuation strength T is estimated via the variance $2\hat{T}\delta t$ of the residuals to the regression, which gives an estimate $\hat{\beta} = 1/\hat{T}$ of the inverse 'temperature' β in the Boltzmann distribution. The non-dimensional combinations $\hat{\beta}\hat{J}$, $\hat{\beta}\hat{a}$ and $\hat{\beta}\hat{b}$ can then be directly compared with the estimates obtained using the distribution-fitting method.

Though SDE discretization independently gives both temperature and coupling constants, it is likely to possess greater intrinsic bias than distribution fitting. Discretization was the only method open for the full model, as the SDE steady state cannot be solved analytically. However, since the reduced model allows for distribution fitting, coupling constant values obtained using that method are preferable, with SDE discretization functioning as an independent verification.

6   One-dimensional geometries

As well as the square and triangular lattices discussed in the main text (Figs. 1 and 3), we also performed experiments on lines of connected vortices (Supplementary Fig. 6). As the finite-circumference
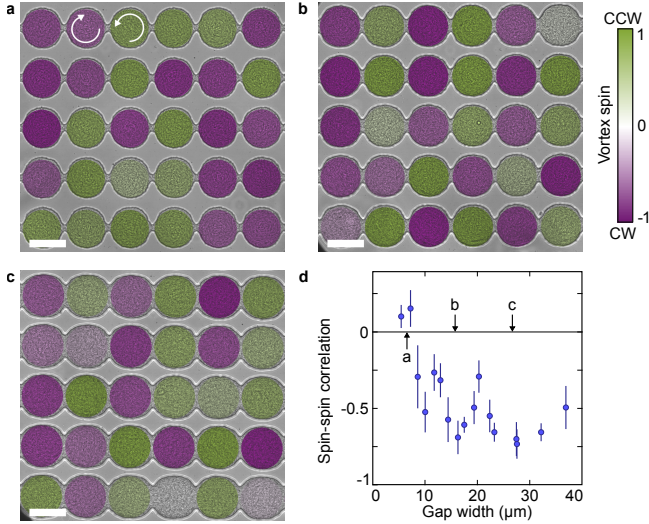
Supplementary Figure 6 – **One-dimensional lattices adopt antiferromagnetic states. a**, At the smallest gap widths, vortices interact weakly resulting in strong but randomly oriented circulation. Gap width $7\,\mu$m. **b,c**, Intermediate and large gaps show strong antiferromagnetic order. Gap widths 16 and $28\,\mu$m. False colour in **a–c** denotes measured vortex spin. Scale bar: $50\,\mu$m. **d**, The spin–spin correlation χ shows the antiferromagnetic state to be largely favoured in lines of cavities. Each point represents an average over ≥ 5 movies in $3\,\mu$m bins at $1.5\,\mu$m intervals; vertical bars indicate standard errors (Methods).

pillars are no longer present in a line of vortices, it is not clear whether the same edge-current-mediated ferromagnetism should be expected. Indeed, we did not observe significant ferromagnetic behaviour at any gap sizes (Supplementary Fig. 6d), suggesting that it is difficult to maintain the single long, uniform edge current that would be necessary for a positively-correlated state. Furthermore, experiments performed on isolated pairs of vortices support these results, in which 76% of the vortex pairs adopted an antiferromagnetic state (out of 34 pairs) with gap sizes between $20\,\mu$m and $38\,\mu$m.

7 Model generalizations

There are more general forms of the model in Eq. (2) which preserve at least some form of local equilibrium. These add flexibility through further couplings or fields at the expense of increased complexity. Though we did not find a need for any further generality, they cannot necessarily be disregarded *a priori*, which we discuss further here.

7.1 Cross-coupled models with frictional dissipation

One generalization of Eq. (2) is to add dissipative cross-couplings. Write $\mathbf{X} = (\mathbf{V}, \mathbf{P})$ for the concatenation of the vectors $\mathbf{V}$ and $\mathbf{P}$. In this formalism, Eq. (2) reads

$$dX_i = -\frac{\partial H}{\partial X_i}dt + \sqrt{2T_i}dW_i, \tag{S8}$$

where T_i is T_v or T_p as appropriate and the W_i are uncorrelated Wiener processes as before. (Repeated indices do not imply summation.) However, in general, we need not have diagonal coupling to derivatives of H. We could instead write[4]

$$dX_i = -\sum_j M_{ij}\frac{\partial H}{\partial X_j}dt + \sum_j m_{ij}\sqrt{2T_j}dW_j,$$

where the M_{ij} are the components of a more general coupling matrix, and $\mathbf{m}$ is the square-root matrix such that $\mathbf{m}^2 = \mathbf{M}$. Onsager reciprocity would then demand $M_{ij} = M_{ji}$ if the vortex spins and pillar flows were relaxing to a true thermodynamic equilibrium with $T_v = T_p$.

The simplest form of this generalization would be to posit a constant coupling between a vortex V_i and the gradients $\partial H/\partial P_j$ of its neighbouring pillars P_j, plus the corresponding reverse coupling. However, a single bacterial vortex experiences most frictional dissipation against the confining upper and lower walls of the cavity, rather than against the much smaller and more porous contact area of the edge currents. Similarly, a single pillar edge current experiences most friction against the solid
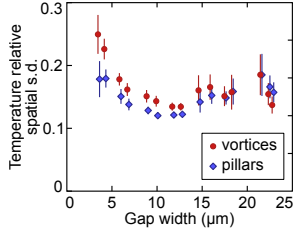
Supplementary Figure 7 – Vortices and pillars show low variability in their individual fluctuation strengths. Relative standard deviations ρ_v and ρ_p of per-site temperatures for vortices (red circles) and pillars (blue diamonds), as defined in the text, are small across gap sizes, only rising at the smallest gaps before the antiferromagnetic–ferromagnetic transition.

pillar walls rather than the porous vortex boundary. This implies that vortex–pillar frictional couplings through a non-diagonal matrix M_{ij} are small, and for this reason we have neglected them here. Indeed, including such couplings would add further parameters to fit in an already strongly fluctuating system, necessitating much more data to statistically distinguish these parameters from zero.

7.2 Spatially variable temperature

Another generalization would be to regard each vortex (and pillar) as possessing its own intrinsic temperature, introducing spatial dependence to the fluctuations. In this scenario, Eq. (S8) would still hold but with the vector of temperatures T_i now no longer constrained to be T_v or T_p. Since the random fluctuations are likely the result of microscopic cell–cell interactions, similar to Brownian motion, temperature variation would be driven by inhomogeneous initial conditions of the suspension, whereby differences in cell or oxygen concentration across the grid of chambers could induce some vortices to fluctuate with greater strength than others. These temperature inhomogeneities may then equilibrate on a time scale beyond that of the experiments due to poor inter-cavity mixing of cells, particularly at the smallest gap sizes. However, provided the fluctuations are zero-mean, inhomogeneous vortex and pillar temperatures should not have a strong effect on the parameters inferred by the linear regression method described in Section 2.

To gauge the extent of any such inhomogeneities, we computed the per-site fluctuation strength T_i as the variance of the residuals to the regression fit for each individual vortex or pillar i. We then computed the relative spatial standard deviations ρ_v and ρ_p for vortices and pillars as $\rho_{\{v,p\}} = \sqrt{\mathrm{Var}_{\{v,p\}} T_i}/T_{\{v,p\}}$, where T_v and T_p are the overall vortex temperatures as in Section 2. This gives a measure of spatial variability suitable for comparison between experiments. For most gap sizes, ρ_v and ρ_p averaged between 0.1 and 0.2, with ρ_v only rising above 0.2 at the smallest gap sizes before the antiferromagnetic–ferromagnetic transition (Supplementary Fig. 7). This suggests that the bulk of any variability is indeed driven by inhomogeneous initial conditions which do not dissipate quickly at small gap sizes. Though these values do indicate non-trivial spatial variability, they are not great enough to warrant detailed inclusion into our model as they would likely not have a great impact on the transition dynamics observed in simulations.

References

[1] Higham, D. J. An algorithmic introduction to numerical simulation of stochastic differential equations. *SIAM Rev.* **43**, 525–546 (2001).

[2] Hänggi, P. Generalized Langevin equations: A useful tool for the perplexed modeller of nonequilibrium fluctuations? In Schimansky-Geier, L. & Pöschel, T. (eds.) *Stochastic Dynamics*, vol. 484 of *Lecture Notes in Physics*, 15–22 (Springer, Heidelberg, 1997).

[3] Dunkel, J. & Hänggi, P. Relativistic Brownian motion. *Phys. Rep.* **471**, 1–73 (2009).

[4] Español, P. Statistical mechanics of coarse-graining. In Karttunen, M., Lukkarinen, A. & Vattulainen, I. (eds.) *Novel Methods in Soft Matter Simulations*, vol. 640 of *Lecture Notes in Physics*, 69–115 (Springer, Heidelberg, 2004).